SIF-based fracture criterion of rock-concrete interface and its application to the prediction of cracking paths in gravity dam

Dong, Wei; Song, Shenzhen; Zhang, Binsheng; Yang, Dong

Published in:
Engineering Fracture Mechanics

DOI:
10.1016/j.engfracmech.2019.106686

Publication date:
2019

Document Version
Author accepted manuscript

SIF-based fracture criterion of rock-concrete interface and its application to the prediction of cracking paths in gravity dam

Wei Dong[1,*], Shenzhen Song[2], Binsheng Zhang[3], Dong Yang[4]

[1]Professor, State Key Laboratory of Coastal and Offshore Engineering, Dalian University of Technology, Dalian 116024, P. R. China. E-mail: dongwei@dlut.edu.cn

*Corresponding author

[2]Postgraduate student, State Key Laboratory of Coastal and Offshore Engineering, Dalian University of Technology, Dalian 116024, P. R. China. E-mail: songsz@mail.dlut.edu.cn

[3]Professor, Department of Civil Engineering and Environmental Management, School of Computing, Engineering and Built Environment, Glasgow Caledonian University, Glasgow G4 0BA, Scotland, United Kingdom. E-mail: Ben.Zhang@gcu.ac.uk

[4]PhD student, Department of Architecture and Civil Engineering, City University of Hong Kong, Tae Chee Avenue, Kowloon, Hong Kong, China. E-mail: dongya2222-x@my.cityu.edu.hk

Abstract

Experimental tests were conducted on the composite rock-concrete specimens with granite, sandstone, and C30/C50 concrete to study the interfacial fracture process under three-point bending and four-point shear conditions. A unified interfacial crack initiation criterion expressed by the stress intensity factors (SIFs) was fitted by the SIFs corresponding to the interfacial crack initiation based on the experimental data. By combining with the fictitious crack model, the crack initiation criterion can be transformed into the crack propagation criterion by considering the contributions of the cohesive forces in the fracture process zone. By assessing the relationships of the interfacial propagation criterion and the maximum circumferential stress criteria of the rock and concrete, the potential interfacial crack propagation paths can be predicted. Furthermore, numerical analyses were carried out by introducing these criteria to simulate the complete fracture process of the rock-concrete interface, where the predicted *P-CMOD* curves and crack trajectories showed good agreements with the experimental data. Finally, by taking a classic gravity dam in practical engineering as an example, the effects of the water levels, initial crack length and crack propagation length on the fracture behaviour of concrete, rock and their interface were investigated. The whole fracture processes for various fracture parameters of the rocks, concretes and their interfaces were simulated numerically. The results indicated that the employed method was effective for the safety assessment of the gravity dam and the application of these propagation criteria is convenient because only the initial fracture toughnesses of the rocks, concretes and their interfaces are required.

Keywords: rock-concrete interface; stress intensity factors; initial fracture toughness; crack propagation criterion; gravity dam

1. Introduction

Concrete gravity dams play very significant roles in flood control, environmental conservation and power generation. In the stability analyses of gravity dams, sliding along a compressed discontinuity [1,2], and crack initiation and propagation along the interface [3,4] are understudied topics. In practice, many factors, including construction process, curing conditions, alkali aggregate reactions, hydrostatic loading, etc., could trigger the initiation of the interfacial cracks between rock foundations and concrete dams. The interfacial cracks are generally regarded as potential safety hazards to concrete dams because these cracks could propagate along different paths under various loading situations [3,5-7] and govern the failure modes of these dams. In order to ensure safe operation of the dams in service, it is of significant importance for academic and engineering communities to investigate the interfacial fracture process and predict the failure modes of the concrete structures constructed on the rock foundations.

The bonding characteristics of the rock-concrete interfacial cracks have a close correlation with crack propagation paths [8]. The interfacial uniaxial tensile strength f_t, the fracture energy G_f and the fracture toughnesses K_{iC} (i = 1, 2) are important mechanical and fracture parameters for evaluating the interfacial bonding properties. Here, K_{1C} and K_{2C} are the fracture toughnesses under mode-I and mode-II fractures, respectively. These parameters are influenced by the roughness degree R_a at the interface [2,9,10] and are approximately linearly correlated with R_a. Meanwhile, the mode-mixity ratio (K_2/K_1), which reflects the stress status at the interfacial crack tip [1,11], showed a significant effect on the potential crack propagation paths [6,11-13], i.e. (1) the interfacial crack always propagates along the interface, (2) the interfacial crack kinks into the base material after partly propagating along the interface, and (3) the interfacial crack kinks into the base material once its

initiation. Case (1) usually occur at a low mode-mixity ratio [6,14], while cases (2) and (3) are more likely to occur at high mode-mixity ratios [5].

In order to investigate the patterns of interfacial crack propagation, many experimental studies were carried out and several interfacial fracture criteria were proposed [11,12]. These criteria can be divided into three categories, namely stress-based [15], energy-based [16,17], and stress intensity factor (SIF)-based [3,6,10,11,14,18]. The stress-based criteria can effectively solve the stress concentration at the crack tip, and have been introduced to determine interfacial crack propagations and predict crack trajectories in the fracture analyses with respect to mode-I dominated [3,6] and mixed mode [5-7,11] fracture criteria. It should be noted that for the mode-I dominated fracture criteria, it usually assumed that the crack always propagates along the interface without branching. However, the scenario is different for the mixed mode fracture due to various potential propagation paths [5]. Therefore, based on the regression on the experimental data, Dong et al. [7] proposed a mixed mode criterion for the rock-concrete interfacial fracture by introducing the interfacial initial fracture toughness of mode-I, K_{1C}^{ini}, to determine three potential crack propagation modes.

However, the abovementioned mixed mode criterion was derived from the experiment, where only C30 concrete and granite were employed. In practice, the value of K_{1C}^{ini} depends on the material properties of the two sides of the interface, as well as the junction of the two materials. It is not clear whether the fitted equation is still appropriate for the interfaces with the various strengths of concretes and different types of rocks. In additon, the mixed mode criterion was only validated by taking a comparion of the predicted results with those from the small-scale samples in the laboratory. The applicability of the criterion has not been verified with respect to the large-scale structures, like

94 concrete gravatiy dams. In the previous research [7] , it has been verified that under mixed mode
95 stress field, the interfacial crack between the rock and concrete would be prone to propagate along
96 the interface with a low K_2/K_1 ratio, and directly kink into the concrete after its initiation under the
97 mixed mode fracture with a high K_2/K_1 ratio. However, it is not clearly clarified whether the crack
98 would kink into the rock foundation for the gravity dams under the practical loading conditions. In
99 addition, linear elastic fracture mechanics (LEFM) has been widely employed to determine the
100 interfacial crack propagation path [3,18,19] in the rock-concrete interfacial fracture analysis.
101 According to the size effect law [20-23], the fracture behaviours in large size structures can be
102 analysed using the LEFM theory because the size for the fracture process zone (FPZ) can be negligible
103 compared to the dimensions of the structures. However, due to the effect of the cohesive force acting
104 on the FPZ, the stress field at the interfacial crack tip will change, leading to the variations of the
105 fracture path even for a large structure with a short FPZ length. Therefore, it is significant to clarify
106 the effect of the cohesive force on the interfacial fracture behaviour, and a comparison of interfacial
107 crack propagation process with/without considering cohesive force should be conducted in further
108 study.

109 In addition, the study on the interfacial crack propagation can be also extended to the failure
110 analysis of concrete at mesoscopic level, where the concrete can be subdivided into mortar,
111 aggregate and their interface. Crack usually occurs at mesoscopic level around those weakest regions,
112 i.e. the interfacial transition zones between aggregates and the surrounding cement paste or matrix
113 [24-26]. The distinct material properties of these randomly distributed mesoscopic phases will
114 significantly affect the crack initiation location, propagation path, failure mode and macroscopic
115 response. For an in-depth insight into the failure mechanism of concrete at mesoscopic level, it is

essential to investigate the crack initiation and propagation at interface and discover the effects of different phases and interfacial properties on the cracking patterns.

In line with this, following the previous study [7], the main aim of this study was to establish the crack propagation criterion for the rock-concrete interfaces formed by various types of concrete and rock. By using the derived criterion from the experiment, the numerical method was used to simulate the interfacial crack propagation process and predict the potential crack propagation paths. Meanwhile, taking a practical gravity dam as an example, the whole fracture behaviour was analysed by introducing the proposed criterion and the effects of materials properties, initial crack length, loading conditions and different criteria on the failure modes were discussed.

2. Experimental program

2.1. Specimen preparation

Two types of composite specimens were tested in this study, including rock-concrete composite prisms and beams, respectively. The dimensions of the composite prisms for the direct tension were 200 mm × 100 mm × 100 mm, where the sizes of both concrete and rock blocks were 100 mm × 100 mm × 100 mm. The beam specimens were prepared for three-point bending (TPB) and four-point shearing (FPS) tests, and had sizes of 500 mm × 100 mm × 100 mm. In the TPB tests, the lengths of the concrete and rock blocks were identical at 250 mm for each block. In order to cover a wide range of mode mixity ratios in the FPS tests, the pre-crack was expected to sustain different combined tension-shear stresses by changing the length of the rock blocks. The lengths of the rock block (L_{rock}) were selected as 225 mm, 235 mm, 240 mm, 245 mm and 250 mm, respectively, in this study. Accordingly, the lengths of the concrete block varied as 275 mm, 265 mm, 260 mm, 255 mm and 250 mm to keep the total lengths of the composite specimens being constant at 500 mm.

The geometries of the composite specimens under the TPB and FPS tests are illustrated in Figs. 1(a) and (b), respectively.

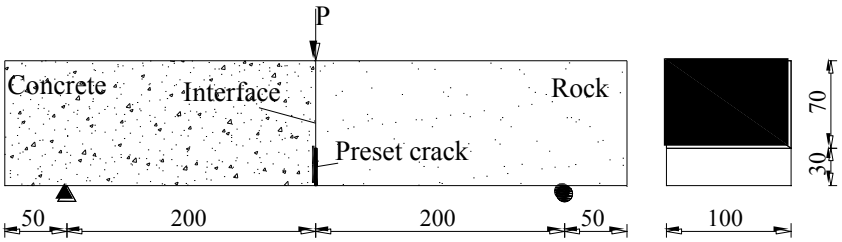

(a) TPB test

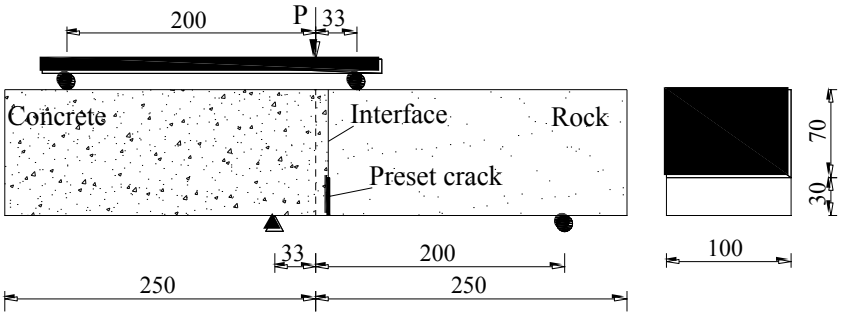

(b) FPS test

Fig. 1. Geometries of the specimens for the TPB and FPS tests (unit: mm).

In order to reduce the dispersion of experimental results and promote the bond strength of the interface, rough interfaces were prepared using artificial groove lines on the contact surfaces of the rock sections. The groove lines were parallel to the diagonal lines of the interfacial cross-section with a depth of 3 mm (see Fig. 2(a)). For each composite beam, the length of the pre-crack, a_0, was 30 mm. To obtain the pre-crack, two layers of polyvinyl chloride (PVC) film were put at the location of the pre-crack on the rock, where one PVC film was pasted on the surface of the rock using glue and the other one was fixed at the same position using cello tape (see Fig. 2(b)). Before testing, the cello tape was pulled out to eliminate the bonding effect between the two layers of the PVC film.

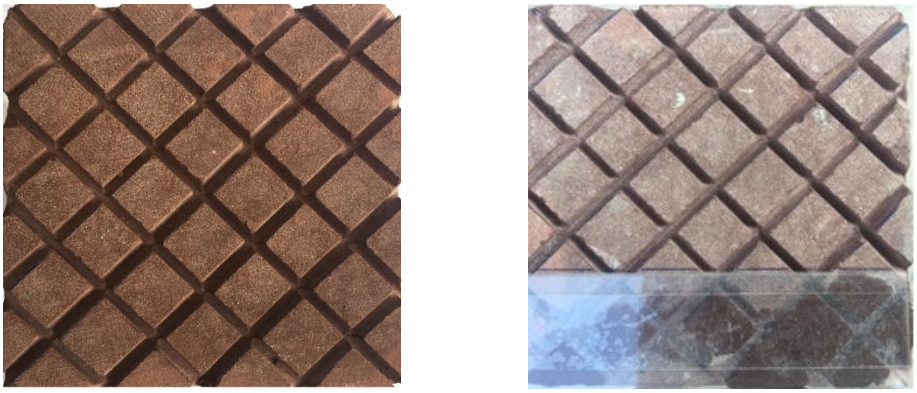

(a) Groove lines **(b)** Pre-crack preparation

Fig. 2. Preparation of rock-concrete interface.

2.2. Material properties

In this experimental study, the granite and sandstone employed were produced in Dalian, Liaoning Province of China. The mixture proportions of C30 and C50 concretes are listed in Table 1. The maximum aggregate sizes for the C30 and C50 concretes were 10 mm and 20 mm, respectively. In addition, 42.5 N and 52.5 N ordinary Portland cements were used for manufacturing the C30 and C50 concretes. The interfaces of the composite specimens were divided into three categories: C50-granite, C30-sandstone and C50-sandstone, denoted as C50-G, C30-S and C50-S. The test specimens were demoulded 2 days after casting and moved into a standard curing room with 23°C and 95% relative humidity (RH) until the age of 28 days.

Table 1 The mix proportions of the concretes (Unit: kg/m^3).

Concrete	Cement	Water	Sand	Aggregate
C30	327 (42.5 N)	195	657	1204 (d_{max} = 10mm)
C50	466 (52.5 N)	214	593	1102 (d_{max} = 20mm)

Note: d_{max} = maximum size of the aggregate.

The measured mechanical properties of the concretes, rocks and rock-concrete interfaces are summarised in Table 2, where E is the elastic modulus, ρ is the density, v is the Poisson's ratio, f_t is the uniaxial tensile strength, f_c is the uniaxial compressive strength, P_{ini} is the initial cracking load, P_{max} is

the peak load, K_{1C}^{ini} is the initial fracture toughness of mode I, and G_{If} is the fracture energy.

Table 2 Material properties of the concretes and rocks.

Materials	E (GPa)	ρ (kg/m^3)	v	f_t (MPa)	f_c (MPa)	P_{ini} (kN)	P_{max} (kN)	K_{1C}^{ini} (MPa·m$^{1/2}$)	G_{If} (N/m)
C30 concrete	29.05	2450	0.236	1.82	47.11	2.327	3.858	0.448	103.61
C50 concrete	32.44	2450	0.175	2.71	57.14	2.825	4.663	0.543	131.67
Sandstone	9.13	2500	0.284	1.65	48.12	1.758	2.123	0.338	120.30
Granite	34.58	2750	0.160	6.59	164.72	9.308	10.233	1.835	219.24

2.3. The TPB and FPS tests

A closed loop servo-controlled MTS (Mechanical Testing and Simulation) testing machine with a capacity of 250 kN was employed for the TPB and FPS tests, as shown in Fig. 3. The tests adopted the displacement-control mode at a displacement rate of 0.024 mm/min. The loading point displacement δ, and the crack mouth opening and sliding displacements, *CMOD* and *CMSD*, were measured by using clip gauges. To measure the initial cracking load, two strain gauges were symmetrically put on both sides of the specimen, 5 mm away from the tip of the pre-crack in the ligament. The strain readings would drop rapidly due to the sudden release of the stored strain energy once the pre-crack initiates. Thus, P_{ini} can be obtained by monitoring the variations of the strains. The experimental results of the TPB and FPS tests are listed in Tables 3 and 4, respectively.

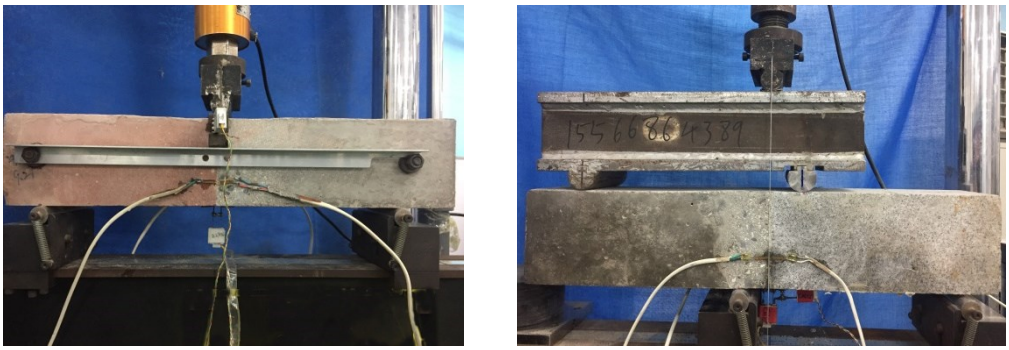

(a) TPB test **(b)** FPS test

Fig. 3. Set-ups for the TPB and FPS tests.

185

186 **Table 3** Experimental results for the TPB tests.

Specimen	P_{ini} (kN)	P_{max} (kN)	f_t (MPa)	K_{1C}^{ini} (MPa·m$^{1/2}$)	G_{If} (N/m)
TPB-C50-G	1.588	2.044	1.588	0.395	31.448
TPB-C30-S	1.152	1.522	1.152	0.297	20.513
TPB-C50-S	1.415	1.796	1.415	0.350	33.205

187

188 **Table 4** Experimental results for the FPS tests.

Specimen	L_{rock} (mm)	P_{ini} (kN)	P_{max} (kN)	K_1^{ini} (MPa·m$^{1/2}$)	K_2^{ini} (MPa·m$^{1/2}$)	$\lvert K_2^{ini}/K_1^{ini}\rvert$	Failure mode
C50-G-225	225	12.245	14.050	0.394	0.140	0.355	I
C50-G-235	235	16.107	20.891	0.343	0.243	0.708	I
C50-G-240	240	20.431	31.782	0.314	0.351	1.118	I
C50-G-245	245	26.162	35.334	0.231	0.505	2.186	I
C50-G-250	250	29.689	40.153	0.049	0.645	13.163	I
C30-S-225	225	8.657	10.825	0.277	0.103	0.372	I
C30-S-235	235	10.816	13.007	0.251	0.173	0.689	K
C30-S-240	240	12.063	16.372	0.211	0.211	1.000	K
C30-S-245	245	13.182	18.457	0.145	0.249	1.717	K
C30-S-250	250	15.897	21.543	0.063	0.317	5.032	K
C50-S-225	225	8.746	11.503	0.287	0.106	0.369	K
C50-S-235	235	9.604	13.374	0.226	0.153	0.683	K
C50-S-240	240	10.308	14.351	0.181	0.180	0.996	K
C50-S-245	245	12.777	15.823	0.143	0.240	1.678	K
C50-S-250	250	13.935	16.622	0.058	0.277	4.776	K

189 **Note:** Failure mode I: the interfacial crack always propagates along interface; Failure mode K: the
190 interfacial crack kinks into rock once its initiation.

191 In Table 3, Specimen TPB-C50-G denotes the TPB specimen with the interface between the
192 C50 concrete and granite. In Table 4, Specimen C30-S-225 denotes the FPS specimen with the
193 interface between C30 concrete and sandstone, and the rock block length L_{rock} = 225 mm. There were
194 two failure modes observed in the tests, i.e. the interfacial crack always propagates along the
195 interface (denoted as mode I), and the interfacial crack kinks into the rock after its initiation (denoted
196 as mode K).

197 The SIFs, K_1 and K_2, of bi-material interface crack were calculated using the displacement

198 extrapolation method [27], and the calculation details can be referred to literature [7]. K_1 and K_2 can
199 be written as K_1^{ini} and K_2^{ini} corresponding to P_{ini}. According to the results for the interface
200 between concrete and sandstone in Table 3, the interfacial bond properties, e.g. f_t, K_1^{ini} and G_{If},
201 increased with the increasing concrete strength. This indicates that the cement mortar with higher
202 strength can provide better bonding at the interface. Meanwhile, if the same strength concrete was
203 selected, the bond surface of the granite can increase the bonding effect compared with that of the
204 sandstone. In addition, only failure mode I was observed for the interfaces between the concrete and
205 granite, i.e. the crack propagated throughout the interface (see Table 4). For the interface between the
206 concrete and sandstone, however, the other failure mode K, where the crack kinked into the
207 sandstone, was also observed (see Table 4). The mechanism for the various interfacial crack
208 propagation paths are to be discussed in the following section.

209 **3. SIF-based crack propagation criterion for rock-concrete interface**

210 *3.1. Introduction of the criterion*

211 According to the previous experimental investigations by Dong et al. [7], the interfacial crack
212 initiation under the mixed mode fracture can be determined from

213 $$\left(\frac{K_1}{K_{1C}^{ini}}\right)^2+\left(\frac{K_2}{1.6\,K_{1C}^{ini}}\right)^2=1 \tag{1}$$

214 The complete fracture process can be considered as the new interfacial crack initiates
215 continually, so that the crack initiation criterion can be employed to determine the interfacial crack
216 propagation by combining with the fictitious crack model [28]. In this manner, Eq. (1) can be written
217 as follows by considering the cohesive force acting on the FPZ.

$$K_{1,2}^{*}=\sqrt{\left(\frac{K_1^{\mathrm{P}}-K_1^{\sigma,\tau}}{1}\right)^2+\left(\frac{K_2^{\mathrm{P}}-K_2^{\sigma,\tau}}{1.6}\right)^2}=K_{1\mathrm{C}}^{\mathrm{ini}} \tag{2}$$

where K_1^{P} and K_2^{P} are the SIFs of modes I and II caused by the external load, while $K_1^{\sigma,\tau}$ and $K_2^{\sigma,\tau}$ are the SIFs of modes I and II caused by the cohesive tensile and shear stresses on the FPZ, σ and τ. Meanwhile, the maximum circumferential stress criterion [3,29] was introduced to determine the kinking of the interfacial crack as follows

$$K_{\mathrm{I,II}}^{*}=\frac{\sqrt{(K_1^{\mathrm{P}}-K_1^{\sigma,\tau})^2+(K_2^{\mathrm{P}}-K_2^{\sigma,\tau})^2}}{2\cosh(\varepsilon\pi)}W_{\mathrm{j}}\left[2\cos\left(\frac{\theta_0}{2}+\gamma\right)-(\cos\theta_0+2\varepsilon\sin\theta_0)\cos\left(\frac{\theta_0}{2}-\gamma\right)+\frac{1}{W_{\mathrm{j}}}\cos\left(\frac{3}{2}\theta_0+\gamma\right)\right]=K_{\mathrm{Ij}}^{\mathrm{ini}} \tag{3}$$

where $K_{\mathrm{Ij}}^{\mathrm{ini}}$ is the initial mode I fracture toughness of material j, j denotes rock or concrete, and θ_0 is the kinking angle [7]. The parameters γ, W_j and ε in Eq. (3) are given as

$$\gamma=\begin{cases}\arctan\left(\dfrac{K_2^{\mathrm{P}}-K_2^{\sigma,\tau}}{K_2^{\mathrm{P}}-K_2^{\sigma,\tau}}\right) & K_1>0\\ \pi+\arctan\left(\dfrac{K_2^{\mathrm{P}}-K_2^{\sigma,\tau}}{K_2^{\mathrm{P}}-K_2^{\sigma,\tau}}\right) & K_1<0\end{cases} \tag{4}$$

$$W_{\mathrm{j}}=\begin{cases}e^{-\varepsilon(\pi-\theta_0)} & j=1\\ e^{\varepsilon(\pi+\theta_0)} & j=2\end{cases} \tag{5}$$

$$\text{bimaterial constant}\quad \varepsilon=\frac{1}{2\pi}\ln\left(\frac{\dfrac{\kappa_1}{\mu_1}+\dfrac{1}{\mu_2}}{\dfrac{\kappa_2}{\mu_2}+\dfrac{1}{\mu_1}}\right) \tag{6}$$

with $$\text{shear modulus}\quad \mu_{\mathrm{i}}=\frac{E_{\mathrm{i}}}{2(1+v_{\mathrm{i}})}\quad (i=1,\ 2) \tag{7}$$

$$\text{elastic constant}\quad \kappa_{\mathrm{i}}=\begin{cases}(3-v_{\mathrm{i}})/(1+v_{\mathrm{i}}) & \text{(plane stress)}\\ (3-v_{\mathrm{i}}) & \text{(plane strain)}\end{cases} \tag{8}$$

where E_{i} is the elastic modulus for material i, and v_{i} is the Poisson's ratio for material i.

By combining Eq. (2) with Eq. (3), the potential propagation of an interfacial crack could be

judged as follows:

(i) If $K_{\mathrm{I,II}}^{*} < K_{\mathrm{Ij}}^{\mathrm{ini}}$ and $K_{1,2}^{*} < K_{1\mathrm{C}}^{\mathrm{ini}}$, the crack does not propagate;

(ii) If $K_{\mathrm{I,II}}^{*} < K_{\mathrm{Ij}}^{\mathrm{ini}}$ and $K_{1,2}^{*} \geq K_{1\mathrm{C}}^{\mathrm{ini}}$, the crack propagates along the interface;

(iii) If $K_{\mathrm{I,II}}^{*} \geq K_{\mathrm{Ij}}^{\mathrm{ini}}$ and $K_{1,2}^{*} < K_{1\mathrm{C}}^{\mathrm{ini}}$, the crack propagates into the material j with a kinking angle θ_0.

3.2. Experimental and numerical verifications

It should be noted that Eq. (1) was derived based on the regression on the experimental results [7], where the composite specimens consisted of C30 concrete and granite. However, it is not clearly clarified whether Eq. (1) would be available for the interfaces with different concrete strengths and rocks. Therefore, three series of composite beams were prepared in this study, where two concrete strengths (C30 and C50), sandstone and granite were selected. According to the experimental results, two failure modes were observed, i.e. the failure mode I with the crack always propagating along the interface and the failure mode K with the interfacial crack kinking into rock after its initiation. The failure modes for all specimens are listed in Table 4. It can be seen that all C50-G series specimens failed under the mode I, while all C30-S and C50-S series specimens failed under the mode K except C30-S-225 series specimens. Fig. 4 illustrates the failure modes of all composite specimens in the experimental study.

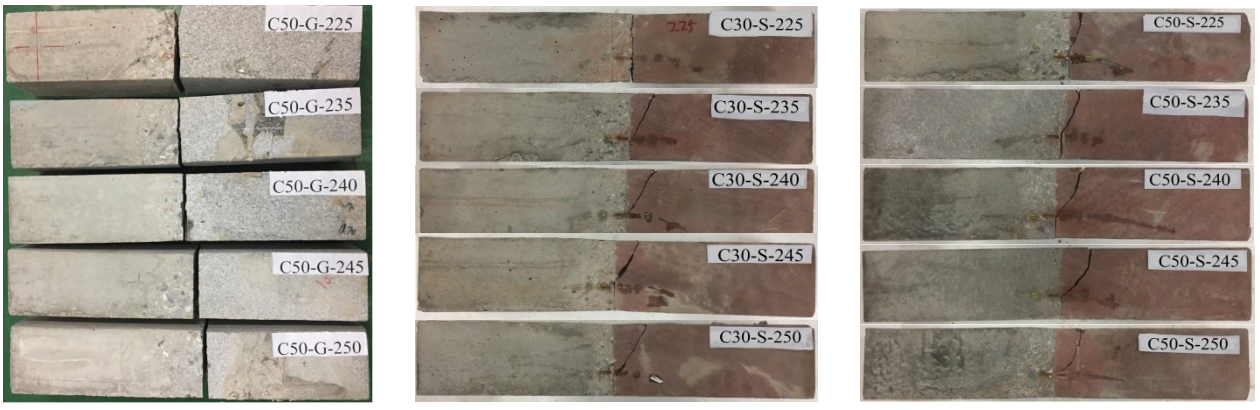

(a) C50-G series specimens **(b)** C30-S series specimens **(c)** C50-S series specimens

Fig. 4. Failure modes of the composite rock-concrete specimens.

Since Eq. (1) represents the criterion for determining the interfacial crack initiation, the points of the normalised terms $K_1^{\text{ini}} / K_{1\text{C}}^{\text{ini}}$ and $K_2^{\text{ini}} / K_{1\text{C}}^{\text{ini}}$ for the C50-G and C30-S-225 series specimens could be employed to fit the initiation equation of the interfacial crack. Accordingly, the points with coordinates of $K_2^{\text{ini}} / K_{1\text{C}}^{\text{ini}}$ and $K_1^{\text{ini}} / K_{1\text{C}}^{\text{ini}}$ for various interfaces are shown in Fig. 5, indicating good agreements with Eq. (1), though only two groups of points were provided for the C30-S series specimens. Therefore, it seems that the rock-concrete interfacial initiation criterion was not affected by the concrete strength and types of rock, i.e. Eq. (1) can be used to determine the rock-concrete interfacial initiation for a wide application.

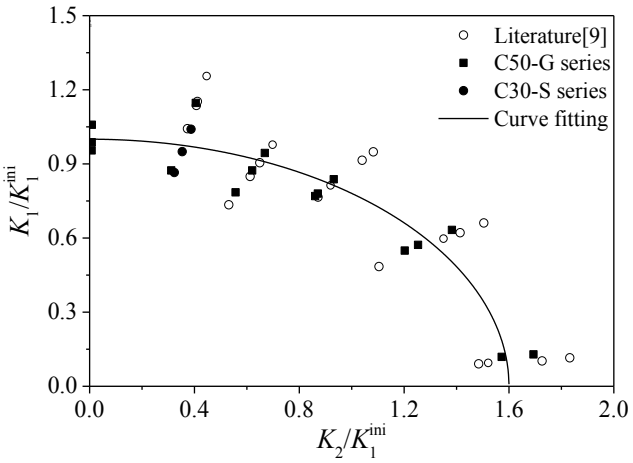

Fig. 5. Fitting curve with the experimental data

Fig. 6 shows the $K_1 - K_2$ relationships of the criteria with $K_{\text{I,II}}^{*} = K_{\text{Ij}}^{\text{ini}}$ for the rocks and $K_{1,2}^{*} = K_{1\text{C}}^{\text{ini}}$ for the interface, where the curves of $K_{\text{I,II}}^{*} = K_{\text{Ij}}^{\text{ini}}$ for granite and sandstone can be determined using Eq. (3) and the curves of $K_{1,2}^{*} = K_{1\text{C}}^{\text{ini}}$ for the interfaces can be determined by Eq. (2). It should be noted that according to the experimental design in this study, the interfacial cracks under the FPS loading shown in Fig. 3(b) cannot propagate into the concrete. Therefore, only the relationships between the rocks and interfaces were discussed here. It can be seen from Fig. 6 that the curve of

$K^*_{\mathrm{I,II}} = K^{\mathrm{ini}}_{\mathrm{Ij}}$ = 1.835 MPa·m$^{1/2}$ for the granite was always outside those of $K^*_{1,2} = K^{\mathrm{ini}}_{\mathrm{1C}}$ = 0.297 MPa·m$^{1/2}$, 0.350 MPa·m$^{1/2}$ and 0.395 MPa·m$^{1/2}$ for the rock-concrete interfaces. This indicates that for the C50-G series specimens under any loading conditions, the crack would not propagate into the granite from the interfaces. This has also been validated by the experimental failure modes of the C50-G series specimens as shown in Fig. 4(a).

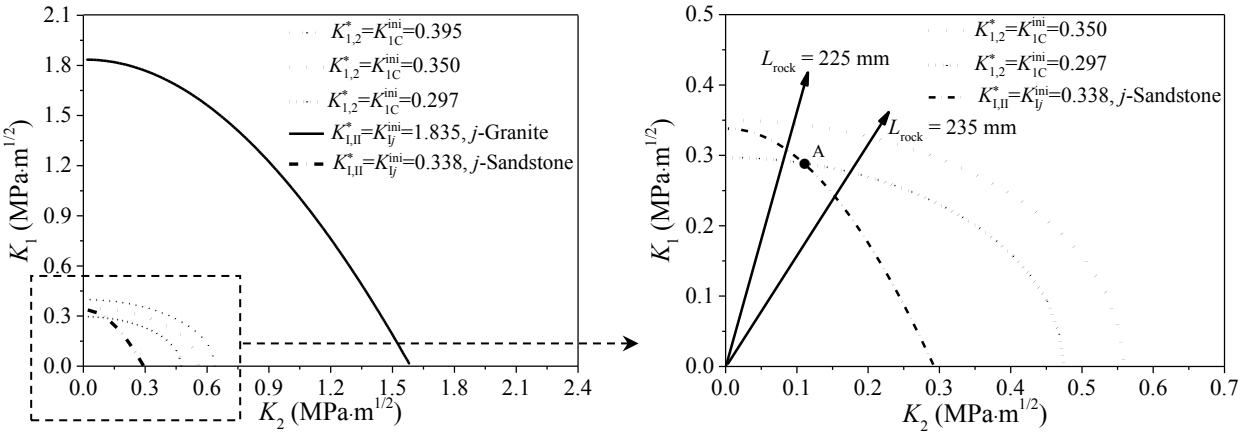

(a) Concrete-granite interface **(b)** Concrete-sandstone interface

Fig. 6. Relationships between $K^*_{1,2} = K^{\mathrm{ini}}_{\mathrm{1C}}$ and $K^*_{\mathrm{I,II}} = K^{\mathrm{ini}}_{\mathrm{Ij}}$ for different interfaces.

Similarly, the curve at $K^*_{1,2} = K^{\mathrm{ini}}_{\mathrm{1C}}$ = 0.350 MPa·m$^{1/2}$ for the interface of the C50-S series specimens was always outside the curve at $K^*_{\mathrm{I,II}} = K^{\mathrm{ini}}_{\mathrm{Ij}}$ = 0.338 MPa·m$^{1/2}$ for the sandstone (see Fig. 6). This indicates that for the C50-S series specimens under any loading conditions, the interfacial crack could propagate into the sandstone after its initiation. This has also been validated by the experimental failure modes of the C50-S series specimens as shown in Fig. 4(c).

In contrast, there was an intersection point between the curve at $K^*_{\mathrm{I,II}} = K^{\mathrm{ini}}_{\mathrm{Ij}}$ = 0.338 MPa·m$^{1/2}$ for the sandstone and the curve at $K^*_{1,2} = K^{\mathrm{ini}}_{\mathrm{1C}}$ = 0.297 MPa·m$^{1/2}$ for the C30-S series specimens, corresponding to the K_2/K_1 ratio of 0.565 (see Point A in Fig. 6). Therefore, the interfacial crack could directly initiate and propagate into the sandstone when $K_2^{\mathrm{ini}} / K_1^{\mathrm{ini}} < 0.565$, but would initiate and

propagate along the interface when $K_2^{ini} / K_1^{ini} > 0.565$. According to the calculated results listed in Table 4, the ratio $K_2^{ini} / K_1^{ini} = 0.376 < 0.565$ for the C30-S-225 series specimens, indicating that for those specimens, the interfacial crack would initiate and propagate along the interface. For the others C30-S series specimens, the interfacial crack would propagate into the sandstone after its initiation. This has been validated by the experimental failure modes of the C30-S series specimens as shown in Fig. 4(b).

The numerical analyses based on the fictitious crack model [30] were carried out to verify the applicability of this criterion. In this study, ANSYS FE code was employed to simulate the complete process of crack propagation under the TPB and FPS loading conditions, with the flow chart shown in Fig. 7. In the fracture analysis, a singular element was used to calculate the SIF at the crack tip. Because high-stress gradients exist in the region around the crack tip, special attention should be paid to that region. Therefore, a circle was set at the tip of the crack, where the crack tip is the centre of the circle and the radius of the circle was 1 mm for the beam specimens. Meanwhile, the first row of elements around the crack tip had a radius of 1/6 mm, and their mid-side nodes were placed at the quarter points, with a radius of 1/24 mm. A re-meshing method [31] was used in the simulation when a new crack path with a propagated length was developed. Taking Specimen C30-S-245 under FPS as an example, different fracture stages under loading are shown in Fig. 8.

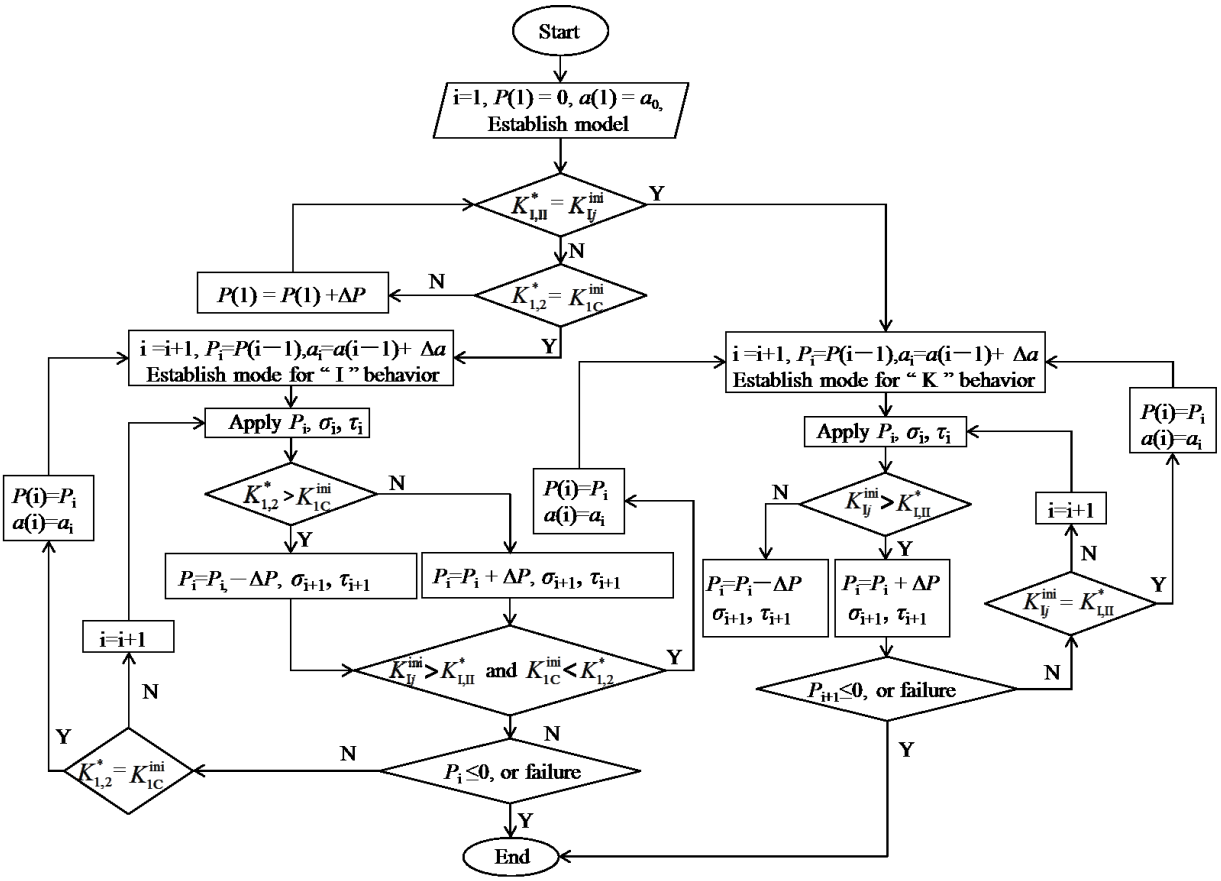

Fig. 7. Simulation flow chart for crack propagation at interface.

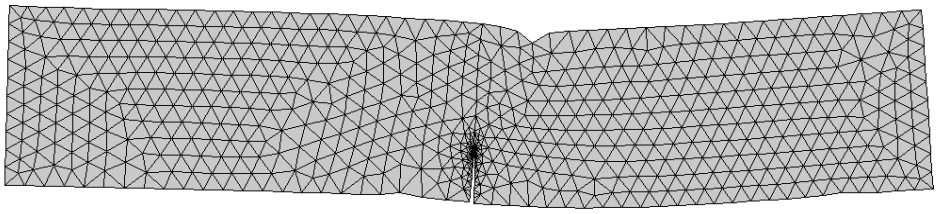

(a) Crack initiation

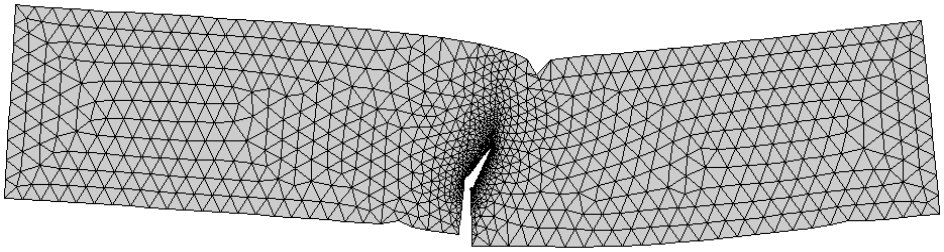

(b) Unstable propagation

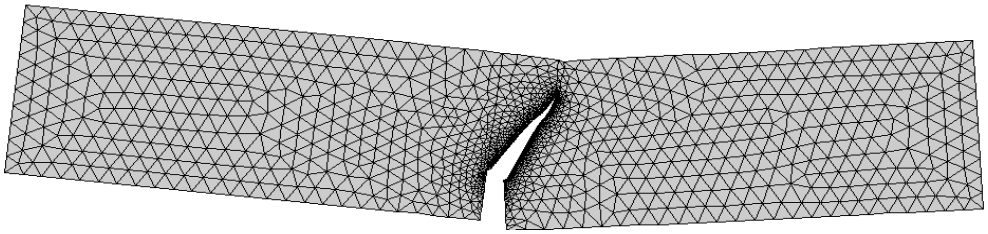

(c) Failure

Fig. 8. Deformed meshes of Specimen C30-S-245 at different fracture stages.

The numerical simulation process is summarised as follows.

1. Establish the FE model with an initial crack length a_0 and apply the load $P(i)$ ($i = 1, 2, \ldots$) until $K^*_{1,2} = K^{\text{ini}}_{1C}$ or $K^*_{I,II} = K^{\text{ini}}_{Ij}$ where i represents the increment of the crack length during iterations.

2. If $K^*_{I,II} = K^{\text{ini}}_{Ij}$, follow Procedures 2(a) to 2(d), otherwise follow Procedure 3.

2(a) Indicate the crack kinks into the sandstone in the direction θ with the increment of Δa, and re-establish model $i = i + 1$ and set $P(i) = P(i–1)$.

2(b) Apply the load P(i) and calculate the cohesive stresses $\sigma(i)$ and $\tau(i)$ according to the cohesive tensile/shear traction – displacement relationships.

2(c) Calculate K^{P}_1, $K^{\sigma,\tau}_1$, K^{P}_2 and $K^{\sigma,\tau}_2$ by adjusting the load $P(i+1) = P(i) \pm n \cdot \Delta P$ ($n = 1, 2, \ldots$) until Eq. (3) is satisfied.

2(d) Repeat Procedures 2(a) to 2(c), until $P(i) \leq 0$ or the specimen failed.

3. If $K^*_{1,2} = K^{\text{ini}}_{1C}$, follow Procedures 3(a) to 3(d).

3(a) Indicate the crack propagates along the interface with the increment of Δa, and re-establish mode $i = i + 1$ and set $P(i) = P(i–1)$.

3(b) Apply the load P(i) and calculate the cohesive stresses $\sigma(i)$ and $\tau(i)$ according to the cohesive tensile/shear traction – displacement relationships.

3(c) Calculate K^{P}_1, $K^{\sigma,\tau}_1$, K^{P}_2 and $K^{\sigma,\tau}_2$ by adjusting load $P(i+1) = P(i) \pm n \cdot \Delta P$ ($n = 1, 2, \ldots$) until Eq. (2) or Eq. (3) is satisfied. If Eq. (3) is satisfied, go to 2(a), while if Eq. (2) is satisfied, go to 3(d).

3(d) Repeat Procedures 3(a) to 3(c), until $P(i) \leq 0$ or specimens failed. Finish.

The interface elements targe168 and conta172 were employed in the simulations. The cohesive forces acting on the FPZ were applied based on the cohesive traction-displacement relationships. The cohesive traction-displacement relationships including tension softening ($w - \sigma$) and shear softening ($w_s - \tau$) are shown in Figs. 9(a) and (b), where w and w_s denote the crack opening and sliding displacements, and σ and τ denote the tension and shear stresses acting on the FPZ. G_{IIf} is the fracture energy for the mode II fracture, which is equal to $2G_{If}$. If the cracking opening/sliding displacements, w and w_s, are larger than the corresponding critical values, w_0 and w_{s0}, the opening/sliding stress-free zones would be formed.

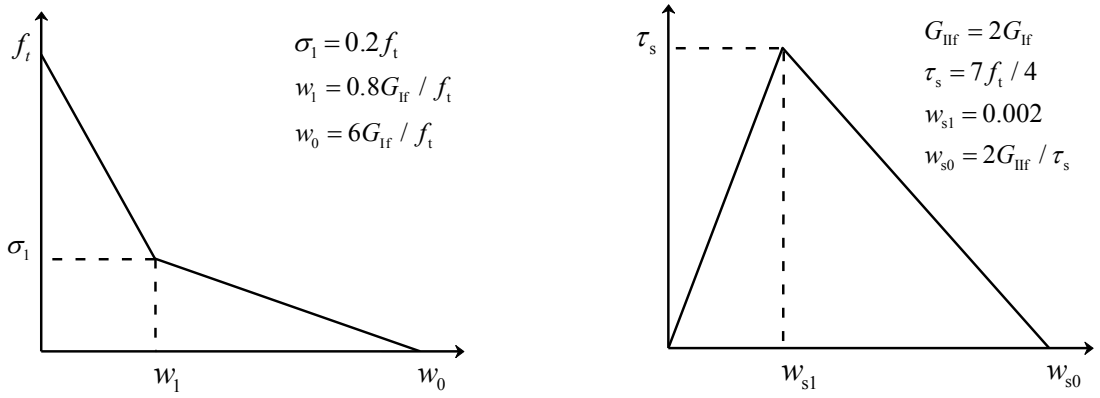

(a) Tension-softening [10] **(b)** Shear-softening [6]

Fig. 9. Cohesive tension traction and shear stress versus displacement relationships.

By performing the iteration process shown in Fig. 7, the complete interfacial crack propagation can be obtained numerically. Taking Specimens TPB-C30-S, C30-S-225, C50-S-240, C50-G-240 as examples, Fig. 10 illustrates the comparisons of the experimental *P-CMOD* curves with the numerical results.

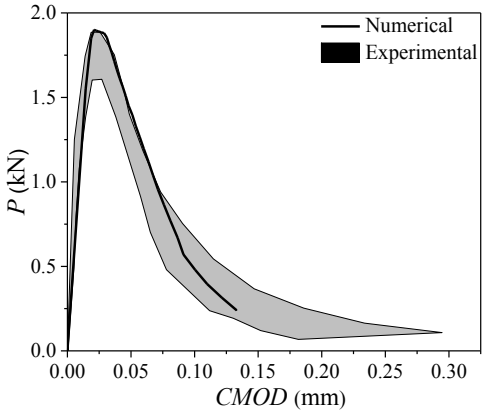

339

340 **(a)** Specimen TPB-C30-S

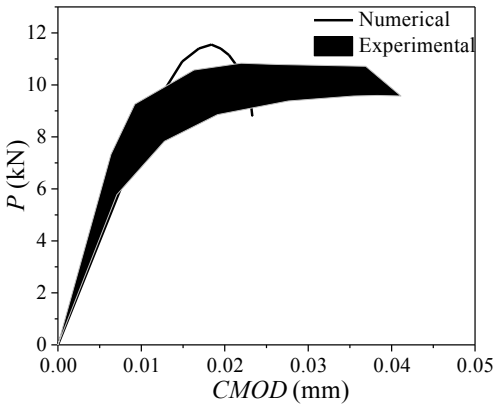

(b) Specimen C30-S-225

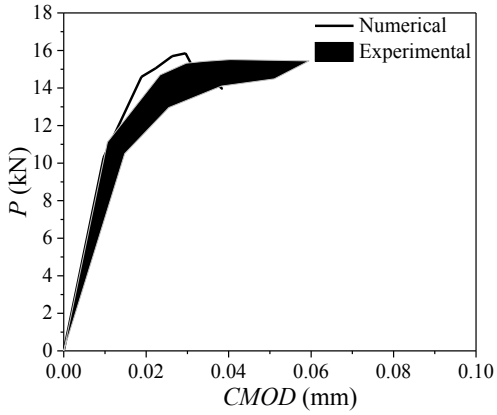

341

342 **(c)** Specimen C50-S-240

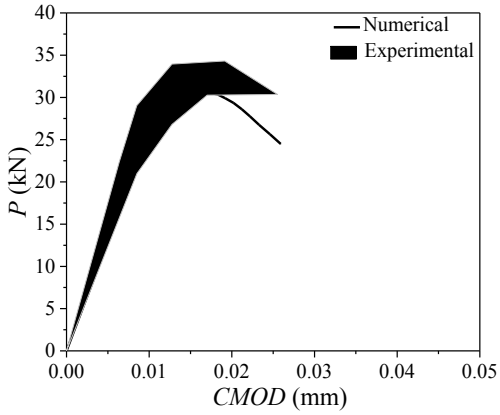

(d) Specimen C50-G-240

343 **Fig. 10.** Comparisons of the *P*-*CMOD* curves on typical TPB and FPS series specimens.

344 For the interfacial crack kinking into the sandstone, Figs. 11(a) and (b) show the comparisons of
345 the crack propagation trajectories between the numerical predictions and experimental measurements
346 for Specimens C30-S-235 and C50-S-250, respectively. By comparing the results in these figures,
347 fairly good agreements can be observed, which verifies the numerical method together with the
348 criterion.

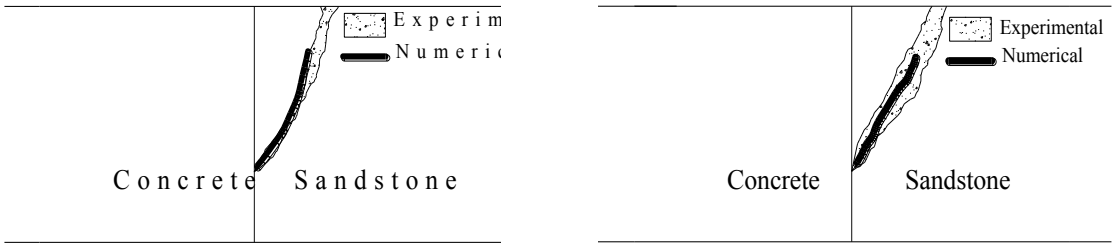

(a) Specimen C30-S-235 **(b)** Specimen C50-S-250

Fig. 11. Comparisons of the crack propagation trajectories.

It is worthwhile to assess whether the interfacial crack for the C30-S-225 series specimens would kink into the sandstone after propagating along the interface. Based on the previous investigations [7], there was a critical value for the ratio $K_2^{\text{ini}} / K_1^{\text{ini}}$ on the curve at $K_{1,2}^{*} = K_{1C}^{\text{ini}}$ for the rock-concrete interfaces. When the ratio $K_2^{\text{ini}} / K_1^{\text{ini}}$ was less than the corresponding critical value, the ratio K_2/K_1 would always decrease as the crack propagated so that the fracture became mode I dominated. In contrast, when the ratio $K_2^{\text{ini}} / K_1^{\text{ini}}$ was greater than the corresponding critical value, the ratio K_2/K_1 would always increase as the crack propagated and the fracture became mode II dominated. According to the numerical results, the critical values of the ratio $K_2^{\text{ini}} / K_1^{\text{ini}}$ for the C50-G, C30-S and C50-S interfaces were determined as 1.22, 1.34 and 1.45, respectively. It should be noted that although the critical ratios were different, they all corresponded to the same geometry with the rock block length of 242 mm. In other words, the critical value of the ratio $K_2^{\text{ini}} / K_1^{\text{ini}}$ was determined by the stress field at the interfacial crack tip. For the composite beams with the same geometry, the same stress field could be obtained under the same loading condition. However, due to the varied properties of the materilas on the two sides of the interfaces, the calculated values of $K_2^{\text{ini}} / K_1^{\text{ini}}$ would be different. Therefore, the stress state at the interfacial crack tip, rather than the critical value of the ratio $K_2^{\text{ini}} / K_1^{\text{ini}}$, can be employed as a constant to determine the interfacial crack propagation path for a wide application.

4. Application of the SIF-based crack propagation criterion to the gravity dam

In order to investigate the applicability of the criterion to practical structures, a classic example of the Greyrock gravity dam in USA [3] was analysed in this study. The cross-sectional geometry of the dam is shown in Fig. 12. Considering the large size for this dam example, the circle mesh at the tip of the crack had a radius of 100 mm. The first row of the elements around the crack tip had a radius of 50/3 mm, and their mid-side nodes were placed at the quarter points, with a radius of 25/6 mm. Three types of loading were applied on the dam, including hydrostatic load, body forces of the dam and uplift pressure inside the crack.

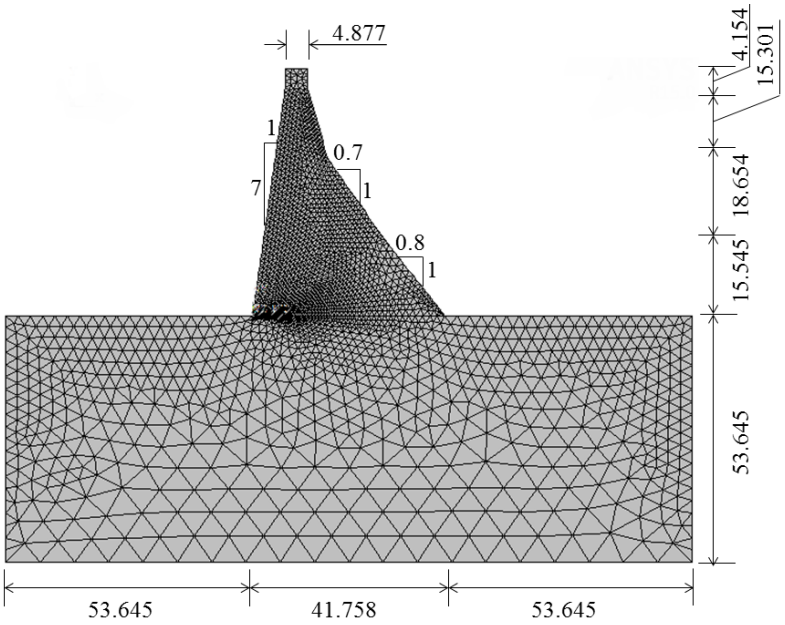

Fig. 12. Finite element model of the Greyrock gravity dam and foundation (unit: m).

The material properties used for the fracture analysis of the dam are listed in Table 5. It should be noted that the values of the parameters E, ρ and v for the concrete and rock, and $K_{\mathrm{IC}}^{\mathrm{un}}$ for the concrete, rock and their interface were quoted from literature [3]. However, the values of the initial fracture toughness $K_{\mathrm{IC}}^{\mathrm{ini}}$ for the concrete, rock and interface would be necessary for the numerical method used in this study. Based on the experimental investigations by Dong et al. [7], the values of

385 the ratio K_{1C}^{ini}/K_{1C}^{un} for the concrete, rock and rock-concrete interface approximately ranged from
386 0.66 to 0.74. Therefore, the ratio of 0.7 was adopted here for the values of K_{1C}^{ini} for the concrete,
387 rock and rock-concrete interface based on the values of K_{1C}^{un}. As a result, 0.726 MPa·m$^{1/2}$, 0.557
388 MPa·m$^{1/2}$ and 0.189 MPa·m$^{1/2}$ were estimated for the initial fracture toughnesses of the concrete,
389 rock and rock-concrete interface. Meanwhile, f_t = 0.656 MPa and G_{If} = 15.12 N/m were also obtained
390 for the rock-concrete interface using the linear interpolation on the experimental data [7].

391 **Table 5** Material parameters used in the fracture analysis of the Greyrock gravity dam.

Material	E (GPa)	ρ (kg/m^3)	v	f_t (MPa)	K_{1C}^{ini} (MPa·m$^{1/2}$)	K_{1C}^{un} (MPa·m$^{1/2}$)	G_{If} (N/m)
Concrete	33.56	2404	0.255	-	0.726	1.044	-
Rock	27.25	0	0.165	-	0.577	0.802	-
Interface	-	-	-	0.656	0.189	0.273	15.12

392

393 *4.1. Interface failure mode*

394 According to the practical loading conditions for the gravity dam in service, the interfacial crack
395 could not propagation into the concrete. Therefore, only the criteria curves for the rock, i.e.
396 $K_{I,II}^{*} = K_{Ij}^{ini}$ (j = rock), and for the interface, i.e. $K_{1,2}^{*} = K_{1C}^{ini}$, were compared as shown in Fig. 13. It
397 can be seen that the curve for $K_{1,2}^{*} = K_{1C}^{ini}$ was outside the curve for $K_{I,II}^{*} = K_{Ij}^{ini}$ (j = rock), so that the
398 interfacial crack would always propagate along the interface.

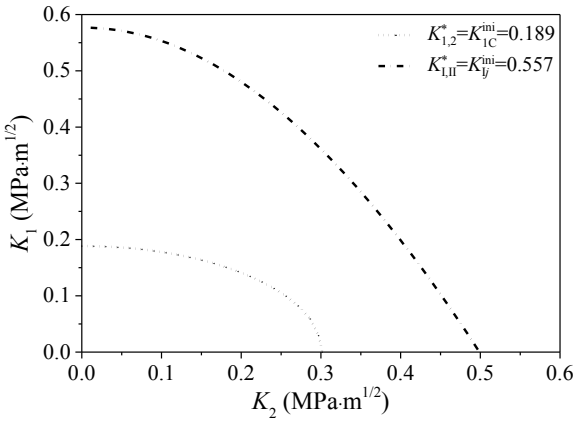

399

Fig. 13. The criteria relationship between $K^{*}_{1,2} = K^{\mathrm{ini}}_{1\mathrm{C}}$ and $K^{*}_{\mathrm{I,II}} = K^{\mathrm{ini}}_{\mathrm{Ij}}$.

Figs. 14(a) and (b) illustrate the variations of K_1 and K_2 under various individual loading conditions, i.e. hydrostatic load (Hydro), body forces (Body) and uplifting pressures (Uplift). The SIFs caused by the combined loading conditions, i.e. the net K_1 and K_2, were shown in these figures. As expected, K_1 caused by the Body had a tendency to hinder the interfacial crack opening, which decreased significantly with the increase the crack length as shown in Fig. 14(a). In addition, the change rate of K_1 caused by the Body was significantly greater than those caused by the Hydro and Uplift, indicating that the effect of the Body became more prominent during the interfacial fracture process. The results agreed well with those by Kishen and Singh [3] based on the LEFM theory. In contrast, K_2 caused by the varied loads did not show obvious variation trends with the increase of the crack length, as shown in Fig. 14(b).

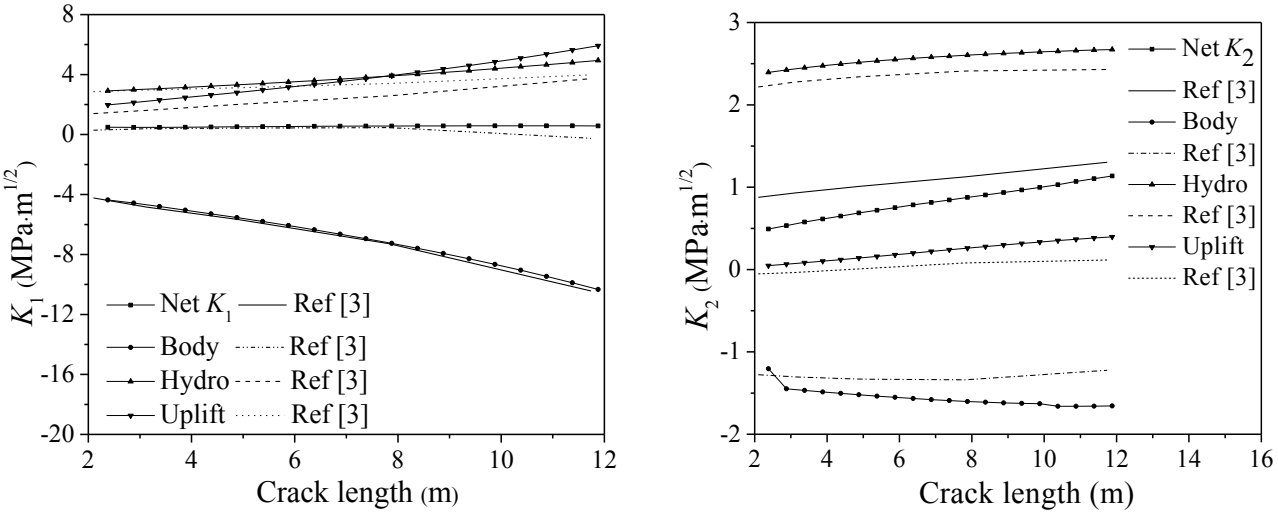

(a) K_1 versus crack length **(b)** K_2 versus crack length

Fig. 14. Variations of the SIFs for individual load conditions (water level of 53.289 m).

In order to intuitively display the change of K_2/K_1, the variations of K_2/K_1 with the increase of the crack length for different water levels, i.e. 53.289 m, 54.289 m, 54.789 m and 55.289 m, are shown in Fig. 15. It can be seen that, the ratio K_2/K_1 at the low water level of 53.289 m presented an

417 obviously increasing tendency, which indicated that K_2 became gradually predominant as the
418 interfacial crack propagated. However, when the water level increased from 53.289 m to 55.289 m,
419 the upward tendency of K_2/K_1 changed to the downward trend, indicating that K_1 became more
420 prominent with the increase of the water level.

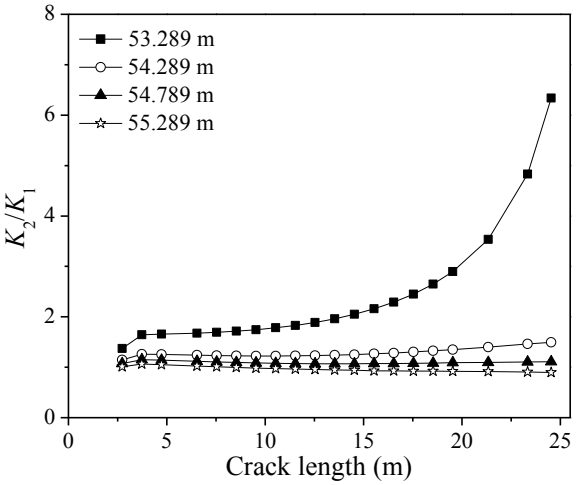

421

422 **Fig. 15.** Variations of K_2/K_1 with crack length.

423 In order to investigate the effects of the initial crack length and water level on the interfacial
424 fracture behaviour, the curves of the SIFs and K_2/K_1 versus the water level under various initial crack
425 lengths, i.e. 2.7 m, 3.5 m, 4.6 m and 6.4 m, are illustrated in Figs. 16(a) and (b). It can be seen from
426 Fig. 16(a) that both K_1 and K_2 increased with the increase of the water level. However, the increase of
427 K_1 was more significant than that of K_2, indicating that the interfacial fracture tended to be mode I
428 dominated with the increase of the water level. A similar tendency can be observed in Fig. 16(b), and
429 the ratio K_2/K_1 approximately kept decreasing with the increase of the water level. Although the
430 values of K_1 and K_2 increased with the increase of the initial crack length, the increments were not
431 prominent. In particular, the values of the ratio K_2/K_1 were hardly affected by the initial crack length,
432 as shown in Fig. 16(b).

433 In summary, the ratio K_2/K_1 was significantly affected by the water level. At the low water level,

e.g. 53.289 m in this study, the ratio K_2/K_1 increased as the interfacial crack propagated. However, it did not vary obviously when the water level was above 54.289 m. Meanwhile, the initial crack length had little impact on the ratio K_2/K_1. Thus, it could be confirmed that the interfacial crack propagation path would be different under the low water level if different concrete, rock and their interface are adopted in practical engineering.

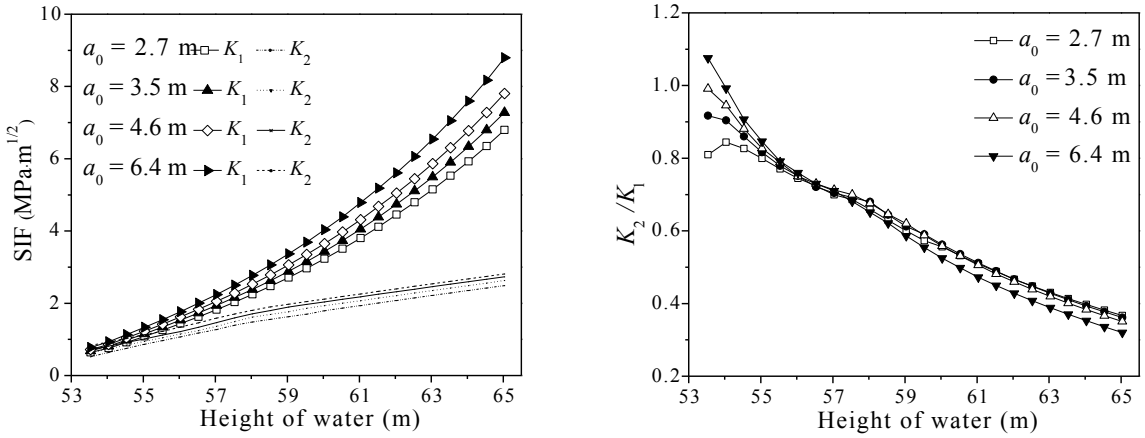

(a) SIF versus water level **(b)** K_2/K_1 versus water height

Fig. 16. Variations of the SIFs with water level and initial crack length.

4.2. Kinking failure mode

According to the experimental study [7], the initial fracture toughness of the rock-concrete interface changed approximately linearly with the roughness degree of the interface. In order to simulate different bonding conditions between the rock and concrete in practical engineering, the values of K_{1C}^{ini} were assumed as 0.125 MPa·m$^{1/2}$, 0.187 MPa·m$^{1/2}$ and 0.350 MPa·m$^{1/2}$, respectively. Meanwhile, sandstone and C30 concrete were selected in this analysis, with the corresponding material properties listed in Table 2. The fracture process was investigated for the water level of 53.289 m, and the initial crack length was set as 2.7 m.

Fig. 17 illustrates the K_1–K_2 relationships for different criteria. Accordingly, there are three

potential crack propagation paths corresponding to different values of K_{1C}^{ini}. When $K_{1,2}^{*} = K_{1C}^{ini} =$ 0.125 MPa·m$^{1/2}$, the criterion curve for the interface would be inside the curve for the rock foundation, so that the crack would always propagate along the interface until failure. In contrast, when $K_{1,2}^{*} = K_{1C}^{ini} =$ 0.350 MPa·m$^{1/2}$, the criterion curve for the interface would be outside the curve for the rock foundation, so that the interfacial crack could kink into the rock foundation after its initiation. Finally, when $K_{1,2}^{*} = K_{1C}^{ini} =$ 0.187 MPa·m$^{1/2}$, there was an intersection point B between the criterion curves for the rock and interface, which corresponded to K_2/K_1 = 1.962. The value of K_2/K_1 corresponding to the crack initiation was 1.370, which was less than 1.962. However, according to the results shown in Fig. 17, the ratio K_2/K_1 would keep increasing as the interfacial crack propagated at the water level of 53.289 m. Therefore, the interfacial crack would first propagate along the interface until the ratio K_2/K_1 reached 1.962. Thereafter, the interfacial crack would kink into the rock foundation, where the predicted crack propagation length along the interface was 13.5 m. Figs. 18(a) to (c) illustrate these three potential interfacial crack propagation paths.

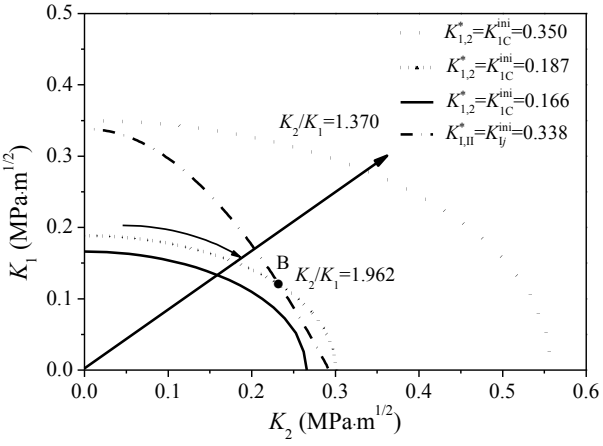

Fig. 17. Determination of the kinking failure modes of the Greyrock gravity dam.

To clarify the effect of the cohesive force on the interfacial fracture behaviour, a comparison of interfacial crack propagation processes with/without considering cohesive force was conducted in this

study.

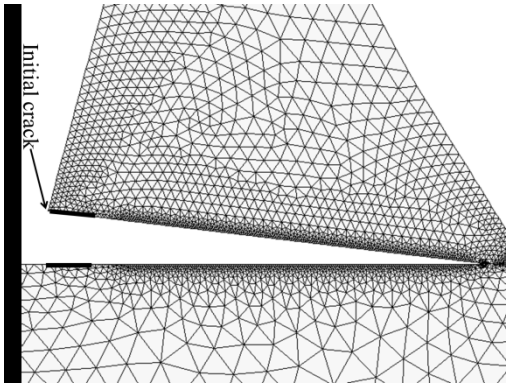

(a) Crack always propagating along the interface

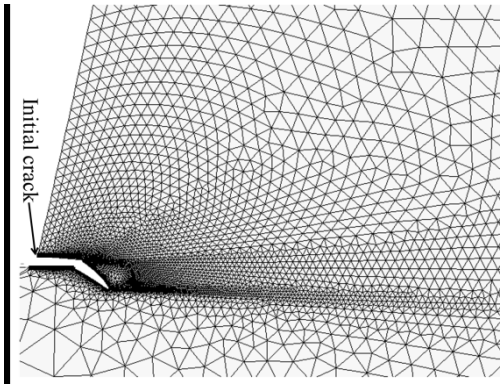

(b) Crack directly kinking into the rock foundation

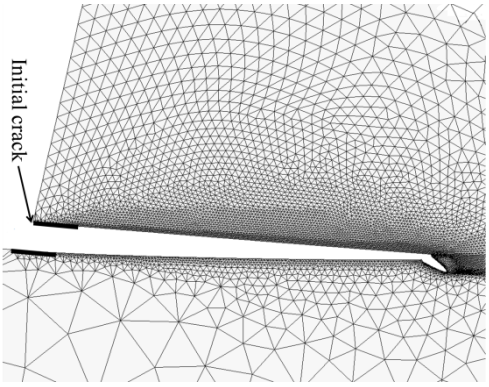

(c) Crack partly propagating along the interface and then kinking into the rock foundation

Fig. 18. Failure modes of the Greyrock gravity dam.

4.3. Effect of the FPZ on the interfacial crack propagation of the gravity dam

In addition, LEFM has been widely employed to determine the interfacial crack propagation path [3,19] in the rock-concrete interfacial fracture analysis. According to the size effect law [20-23], the

fracture behaviors in a large size structure can be analyzed using the LEFM theory because the FPZ size can be negligible compared to the structure dimension. However, due to the effect of the cohesive force acting on the FPZ, the stress field at the interfacial crack tip will change, leading to the variations of the fracture path even for a large structure with a short FPZ length. To clarify the effect of the cohesive force on the interfacial fracture behavior, a comparison of interfacial crack propagation processes with/without considering cohesive force was conducted in this study.

Fig. 19 illustrates the variations of K_2/K_1 with and without considering the cohesive force on the FPZ at the water level of 53.289 m for the Greyrock gravity dam. It can be seen that for the same crack length, the values of K_2/K_1 considering the cohesive force were larger than those without considering the cohesive force. Therefore, the values of K_2/K_1 with/without considering the cohesive force would reach 1.962 with respective to the different crack propagation lengths. As a result, the interfacial crack could kind into the rock foundation for the different crack propagation lengths. Based on the numerical results with and without considering the cohesive force, the crack lengths corresponding to kinking into the rock foundation were determined as 13.5 m and 15.7 m, respectively. Therefore, the interfacial crack propagation path would be predicted inaccurately if the effect of the cohesive force is neglected and the LEFM method is adopted in the interfacial fracture analysis.

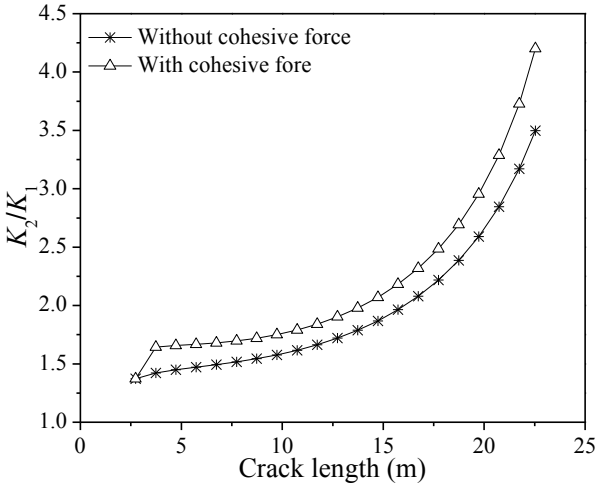

Fig. 19. Variations of K_2/K_1 with crack length

4.4 Applications of different SIF-based crack propagation criteria to the gravity dam

For the SIF-based criteria, there existed different viewpoints on the assessment of the difference between the SIFs caused by the applied load and cohesive stress. One is the mode I dominated SIF criterion, which considers that the interfacial crack would propagate when $K_1 = K_{1C}^{ini}$ [3] (Criterion-I). The second one is the nil SIF criterion, which considers that the interfacial crack would propagate when $K_1 = 0$ [4,32] (Criterion II). The final one is the mixed mode SIF criterion, i.e. the criterion proposed in this paper (Criterion III). In summary, the expressions of these three SIF-based criteria are listed in Table 6. It should be noted that only the crack propagation along the interface was considered in this discussion.

Table 6. Expressions of various SIF-based criteria

Interfacial criterion	Propagation condition
I	$K_1 = K_1^{\mathrm{P}} - K_1^{\sigma,\tau} = K_{1C}^{ini}$
II	$K_1 = K_1^{\mathrm{P}} - K_1^{\sigma,\tau} = 0$
III	$K_{1,2}^{*} = \sqrt{\left(\frac{K_1^{\mathrm{P}} - K_1^{\sigma,\tau}}{1}\right)^2 + \left(\frac{K_2^{\mathrm{P}} - K_2^{\sigma,\tau}}{1.6}\right)^2} = K_{1C}^{ini}$

Fig. 20 illustrates the variations of the K_1 with the crack length under the loading condition at 53.289 m water level, where K_{1C}^{ini} was adopted as 0.189 MPa·m$^{1/2}$. Meanwhile, the variations of K_1 for three criteria with respect to the crack propagation length are also illustrated in the figure. It should be noted that in the case of Criterion III, the crack propagation was dominated by the combination of K_1 and K_2, so that K_1 decreased as the crack propagation. The interfacial crack would not propagation when the variation curve of K_1 intersected with the criteria. Accordingly, the crack propagation lengths based on the three criteria were 24.381 m, 25.564 m and 25.811 m (see Points A, B and C in Fig. 20), respectively. Because K_1 decreased to 0.0324 MPa·m$^{1/2}$ for Criterion III, therefore, the predicted crack propagation lengths using Criteria II and III were very close.

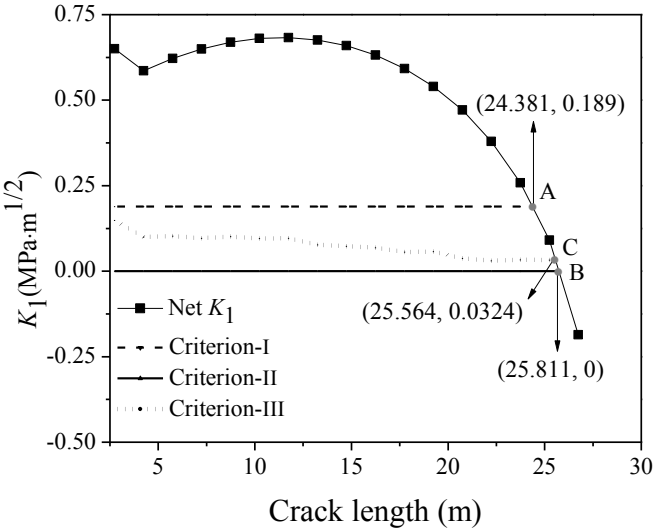

Fig. 20. Variations of K_1 with crack length at water level of 53.289 m

Fig. 21 illustrates the relationships between the SIFs for different criteria, which can qualitatively explain the predicted results shown in Fig. 20. Points A, B and C denote the SIFS corresponding to the crack propagation under Criteria I, II and III, respectively. In the case of Criterion III, the crack propagation is dominated by the combination of mode 1 and 2 fractures. Therefore, the crack would propagate under the SIFs K_1^{ini} and K_2^{ini}, i.e. Point C in Fig. 21. At that

moment, due to $K_{1C}^{ini} > K_1^{ini}$, the crack would not propagate if Criterion I is employed. As a result, the interfacial cracking resistance would be overestimated under Criterion I. Particularly, the larger difference between K_{1C}^{ini} and K_1^{ini}, the lager error would be caused. In other words, the error would increase with the increase of the ratio K_2^{ini}/K_1^{ini}. On the contrary, due to $K_1^{ini} > 0$, the crack has propagated if Criterion II is used. As a result, the interfacial cracking resistance would be underestimated under Criterion I. Accordingly, the error would increase with the decrease of the ratio K_2^{ini}/K_1^{ini}.

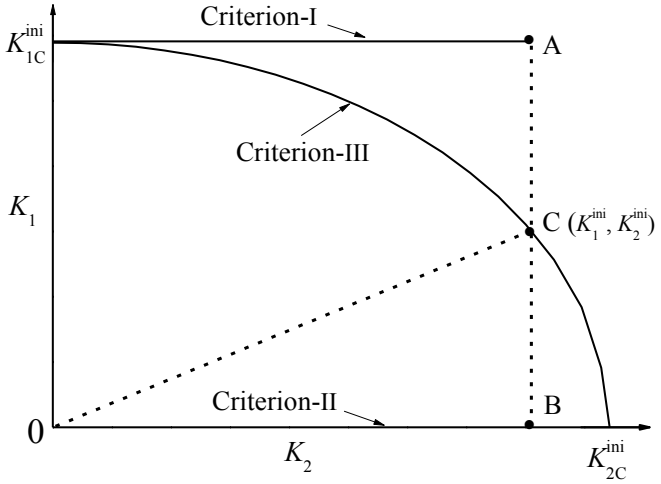

Fig. 21. Relationships of SIFs under different criteria

5. Conclusions

Experimental investigations were first carried out to verify the applicability of the interfacial crack propagation criterion for various categories of concrete strength and rock. The FPS tests with a wide range of mode mixity ratios were conducted on three series of rock-concrete composite beams. Thereafter, numerical analyses were accomplished to simulate the interfacial crack propagation process and predict the potential fracture paths, and validated by comparing the *P-CMOD* curves and cracking trajectories between the experimental and numerical results. Finally, the fracture analyses on a practical gravity dam were performed numerically by applying the interfacial crack propagation

criterion. According to the comprehensive experimental and numerical investigations, the following conclusions can be drawn:

1. The interfacial crack initiation criterion derived from the experimental studies was widely applicable to the interfaces constituted of different categories of rock and concrete with various strength grades. By combing the fictitious crack model, the crack initial criterion can be transformed into the crack propagation criterion by considering the contributions of cohesive forces on the fracture, which can be used to determine the crack propagation along the interface.
2. By assessing the relationships between the interfacial crack propagation and the maximum circumferential stress criteria for the rock and concrete, the potential interfacial crack propagation paths could be predicted. It is convenient to apply the crack propagation criterion in practical engineering because only the initial fracture toughnesses of the rock, concrete and their interface are required. Also, numerical analyses were carried out to simulate the complete interfacial fracture process by introducing these criteria, and the numerical simulations showed good agreements with the experimental results.
3. By taking a practical gravity dam as an example, the complete fracture process of the dam was analysed numerically under the actual loading conditions. Based on the relationships between these criteria, three potential propagation paths existed for the interfacial crack. The stress field at the interfacial crack tip and the initial fracture toughnesses of rock, concrete and their interface had significant effects on the interfacial crack propagation paths. If the initial fracture toughness of the rock was significantly larger than that of the interface, the interfacial crack would always propagate along the interface. If the initial fracture toughness of the rock was significantly smaller than that of the interface, the interfacial crack would kink into the rock foundation after its

initiation. If the initial fracture toughnesses of the rock and interface were similar, the interfacial crack might first propagate along the interface and then kink into the rock foundation, which also depended on the stress field at the interfacial crack tip. In addition, the mode mixity ratio K_2/K_1 increased significantly as the interfacial crack propagated at the low water level, e.g. 53.289 m. In contrast, the ratio K_2/K_1 did not show obvious variations as the interfacial crack propagated if the water level was above 53.289 m. Meanwhile, the initial crack length had little impact on the variations of the ratio K_2/K_1.

4. For the extended study, different values of the initial fracture toughnesses for the rock, concrete and their interface were selected to match the actual case in practice. Three typical interfacial crack propagation paths can be observed, depending on the relationships between these criteria. In addition, the effect of FPZ on the interfacial crack propagation of a gravity dam was explored by comparing the numerical results with and without considering the cohesive force. The introduced cohesive forces increased the ratio K_2/K_1 and led the interfacial crack to kink into the rock foundation with a short propagation length along the interface.

5. Different criteria were employed to predict the interfacial crack propagation length under a constant water level. Compared with the criterion proposed in this study, i.e. Criterion III, the mode 1 dominated criterion, i.e. Criterion I, would overestimate the cracking resistance, and the error would increase with the increase of the ratio $K_2^{\mathrm{ini}}/K_1^{\mathrm{ini}}$. Accordingly, the nil SIF criterion, i.e. Criterion II, would underestimate the cracking resistance, and the error would increase with the decrease of the ratio $K_2^{\mathrm{ini}}/K_1^{\mathrm{ini}}$.

Acknowledgements

The financial supports of the National Natural Science Foundation of China under the grants of

NSFC 51878117, NSFC 51478083 and NSFC 51109026, and the Natural Science Foundation of Liaoning Province of China under the grant of 20170540183 are gratefully acknowledged.

References

[1] Andjelkovic V, Pavlovic N, Lazarevic Z, Nedovic V. Modelling of shear characteristics at the concrete - rock mass interface. Int J Rock Mech Min 2015;76:222-236.

[2] Bassel EI Merabi. Mechanical behavior of cohesive concrete-rock joint at the dam-foundation interface: geometrical and mechanical influence of asperities. Université Grenoble Alpes, 2018.

[3] Kishen JC, Singh KD. Stress intensity factors based fracture criteria for kinking and branching of interface crack: application to dams. Eng Fract Mech 2001;68(2):201-219.

[4] Yao F, Yang ZJ, Hu YJ. An SBFEM-based model for hydraulic fracturing in quasi-brittle materials. Acta Mech Solida Sin 2018;31(12):1-17.

[5] Slowik V, Kishen JC, Saouma VE. Mixed mode fracture of cementitious bimaterial interfaces Part I Experimental results. Eng Fract Mech 1998;60(1):83-94.

[6] Zhong H, Ooi ET, Song C, Ding T. Experimental and numerical study of the dependency of interface fracture in concrete-rock specimens on mode mixity. Eng Fract Mech 2014;124(9):287-309.

[7] Dong W, Dong Y, Zhang B. Rock-concrete interfacial crack propagation under mixed Mode I-II fracture. J Eng Mech 2018;114(6):4018039.

[8] Yuuki R. Simulation analysis of fracture in ceramic/metal bonded joints. Trans Jpn Soc Mech Eng (in Japanese) 1994;60(579):2544-2552.

[9] Tian HM, Chen WZ, Yang DS, Yang JP. Experimental and numerical analysis of the shear behaviour of cemented concrete-rock joints. Rock Mech Rock Eng 2015;48(1):213-222.

[10] Dong W, Wu Z, Zhou X. Fracture mechanisms of rock-concrete interface: experimental and numerical. J Eng Mech 2016;142(7):4016040

[11] Yang S, Song L, Li Z, Huang S. Experimental investigation on fracture toughness of interface crack for rock/concrete. Int J Mod Phys B 2008;22(31&32):6141-6148.

[12] Yuuki R, Liu JQ, Xu JQ, Ohira T. Fracture tests and evaluation of interface crack under mixed mode condition. Trans. Jpn. Soc. Mech. Eng. (in Japanese) 1993;59(557):74-80.

[13] Ryoji Y, Liu J-Q, Xu J-Q, Toshiaki O, Tomoyoshi O. Mixed mode fracture criteria for an interface crack. Eng Fract Mech 1994;47(3):367-377.

[14] Dong W, Yang D, Zhou X, Kastiukas G. Experimental and numerical investigations on fracture process zone of rock-concrete interface. Fatigue Fract Eng M 2017;40(5):820-835.

[15] Červenka J, Kishen JC, Saouma VE. Mixed mode fracture of cementitious bimaterial interfaces Part II Numerical simulation. Eng Fract Mech 1998;60(1):95-107.

[16] Sujatha V, Kishen JC. Energy release rate due to friction at bimaterial interface in dams. J Eng Mech 2003;129(7): 793-800.

[17] Datta D, Tomar V, Varma AH. A path independent energy integral approach for analytical fracture strength of steel-concrete structures with an account of interface effects. Eng Fract Mech 2018;204:246-267.

[18] Benarbia D, Benguediab M. Determination of stress intensity factor in concrete material under Brazilian disc and three-point bending tests using finite element method. Periodica Polytechnica. Engineering. Mech Eng 2015:59(4),199-203.

627 [19] Yang Z, Xu FX. A heterogeneous cohesive model for quasi-brittle materials considering spatially varying random
628 fracture properties. Comput Methods Appl Mech Eng 2008;197:4027-4039.
629 [20] Bažant ZP, Pfeiffer PA. Determination of fracture energy from size effect and brittleness number. ACI Mater J
630 1987;84(6):463-480.
631 [21] Bažant ZP, Kazemi M T. Size effect in fracture of ceramics and its use to determine fracture energy and effective
632 process zone length. J Am Ceram Soc 1990;73(7):1841-1853.
633 [22] Bažant ZP, Planas J. Fracture and Size Effect in Concrete and Other Quasibrittle Materials. CRC Press 1997.
634 [23] Bažant ZP, Yu Q. Universal size effect law and effect of crack depth on quasi-brittle structure strength. J Eng Mech
635 2009;135(2):78-84.
636 [24] Yang ZJ, Li BB and Wu JY. X-ray computed tomography images based phase-field modeling of mesoscopic failure in
637 concrete, Eng Fract Mech 2019;208:151-170.
638 [25] Huang YJ, Yang ZJ, Ren WY, Liu GH and Zhang C. 3D Meso-scale fracture modelling and validation of concrete
639 based on in-situ X-ray computed tomography images using damage plasticity model, Int J Solids Struct
640 2015;67-68:340-352.
641 [26] Su XT, Yang ZJ and Liu GH. Monte Carlo simulation of complex cohesive fracture in random heterogeneous
642 quasi-brittle materials: a 3D study. Int J Solids Struct 2010;47:2336-2345.
643 [27] Nagashima T, Omoto Y, Tani S. Stress intensity factor analysis of interface cracks using X−FEM. Int J Numer Meth
644 Eng 2003;56(8):1151-1173.
645 [28] Wu ZM, Rong H, Zheng JJ, Dong W. Numerical method for mixed mode I−II crack propagation in concrete. J Eng
646 Mech 2013;139(11):1530-1538.
647 [29] Yuuki R, Xu J-Q. Stress based criterion for an interface crack kinking out of the interface in dissimilar materials.
648 Eng Fract Mech 1992;41(5):635-644.
649 [30] Hillerborg A, Modéer M, Petersson P. Analysis of crack formation and crack growth in concrete by means of
650 fracture mechanics and finite elements. Cement Concrete Res 1976;6(6):773-781.
651 [31] Yang Z, Propagation MC, Procedure R. Fully automatic modelling of mixed-mode crack propagation using scaled
652 boundary finite element method. Eng Fract Mech 2006;73(12):1711-1731.
653 [32] Moës N, Belytschko T. Extended finite element method for cohesive crack growth. Eng Fract Mech
654 2002;69(7):813-833.
655
656
657
658
659